JACS
JOURNAL OF THE AMERICAN CHEMICAL SOCIETY
Article
pubs.acs.org/JACS

Resolving the Growth of 3D Colloidal Nanoparticle Superlattices by Real-Time Small-Angle X-ray Scattering

Chenguang Lu,* Austin J. Akey, Clayton J. Dahlman, Datong Zhang, and Irving P. Herman*

Department of Applied Physics and Applied Mathematics, Columbia University, New York, New York 10027, United States

Supporting Information

ABSTRACT: The kinetics and intricate interactions governing the growth of 3D single nanoparticle (NP) superlattices (SLs, SNSLs) and binary NP SLs (BNSLs) in solution are understood by combining controlled solvent evaporation and *in situ*, real-time small-angle X-ray scattering (SAXS). For the iron oxide (magnetite) NP SLs studied here, the larger the NP, the farther apart are the NPs when the SNSLs begin to precipitate and the closer they are after ordering. This is explained by a model of NP assembly using van der Waals interactions between magnetite cores in hydrocarbons with a ~21 zJ Hamaker constant. When forming BNSLs of two different sized NPs, the NPs that are in excess of that needed to achieve the final BNSL stoichiometry are expelled during the BNSL formation, and these expelled NPs can form SNSLs. The long-range ordering of these SNSLs and the BNSLs can occur faster than the NP expulsion.

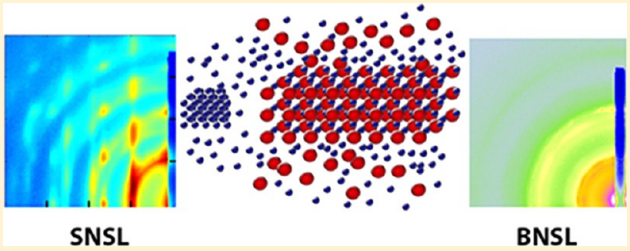

INTRODUCTION

Colloidal nanoparticle (NP) superlattice (SL) metamaterials hold the promise of novel and tunable collective properties due to the periodic NP arrangement.[1−6] One challenge in attaining this goal has been the need to supplant empirical methods of SL development by rational design and fabrication. One approach is through surface modification.[2,4−6] Another is with better control of assembly through improved understanding of kinetics while using NPs with the ligands from growth; these NPs may have the practical advantages[3,7−14] of superior cost, materials availability, and scaling-up potential. We show here that we can understand and presumably control NP assembly better through resolving the kinetics and intricate interactions governing the growth of 3D single NP SLs (SNSLs) and binary NP SLs (BNSLs) in solution by combining controlled solvent evaporation and *in situ*, real-time small-angle X-ray scattering (SAXS). Specifically, we learn how NP size affects the rate of assembly of SNSLs and the mechanism of how coexisting SNSLs and BNSLs form.

The mechanism of the self-assembly of such NPs into 2D and 3D SLs has been addressed by several groups by using *ex situ* methods.[15−20] *In situ* probing techniques, such as AFM, TEM, and SAXS, have also been used,[21−27] most in real time.[21,23−27] However, there has been little real-time analysis of 3D SNSL formation, such as that by optical probing of several SNSLs[7,23] and SAXS of metal NP SNSLs,[25,26] and apparently none of 3D BNSL formation, in part due to challenges in controllably forming 3D SLs. We have developed a multiple solvent system that enables the growth of large and high-quality 3D NP SL metamaterials, with growth rates slow enough for a detailed SAXS study of the kinetics of ordered NP growth. For the systems studied here, we see that when forming SNSLs, the larger the NP, the farther apart are the NPs when they begin to precipitate and the closer they are after ordering. Also, when forming BNSLs of two different sized NPs, the NPs that are in excess of that needed to achieve the final BNSL stoichiometry are expelled during the BNSL formation, and these expelled NPs can form SNSLs. The long-range ordering of these SNSLs and the BNSLs can occur faster than the NP expulsion.

We chose oleic acid-capped iron oxide (magnetite) NPs as a model system for a general analysis of growth because they can be formed with a wide range of diameters (6−15 nm) and high monodispersity[28] and can readily dissolve in common nonpolar solvents at room temperature.

EXPERIMENTAL SECTION

We developed a multiple solvent system consisting of 72% toluene, 22% decane, and 6% dodecane to slow down the critical moments of solvent evaporation during self-assembly after drop casting the NP solution on a Kapton substrate to achieve successful SL formation,[29,30] as well as to permit SAXS analysis at the Brookhaven National Laboratory NSLS Beamline X9A. Figure S1 in the Supporting Information (SI) depicts the chamber we used for real-time SAXS (maintained at 100 Torr during drying for the SLs in Figures 1, 2, and 4, and 300 Torr for those in Figure 3 to slow down the evaporation even more to improve SAXS temporal resolution). See ref 36 and the SI for more details on NP synthesis, SL assembly, and analysis.

RESULTS AND DISCUSSION

Establishing Conditions for Growing SNSLs and BNSLs. SL growth conditions were first established without X-ray probing. Figure 1a shows the SEM images of the

Received: August 7, 2012
Published: October 3, 2012

   dx.doi.org/10.1021/ja307848h | J. Am. Chem. Soc. 2012, 134, 18732−18738

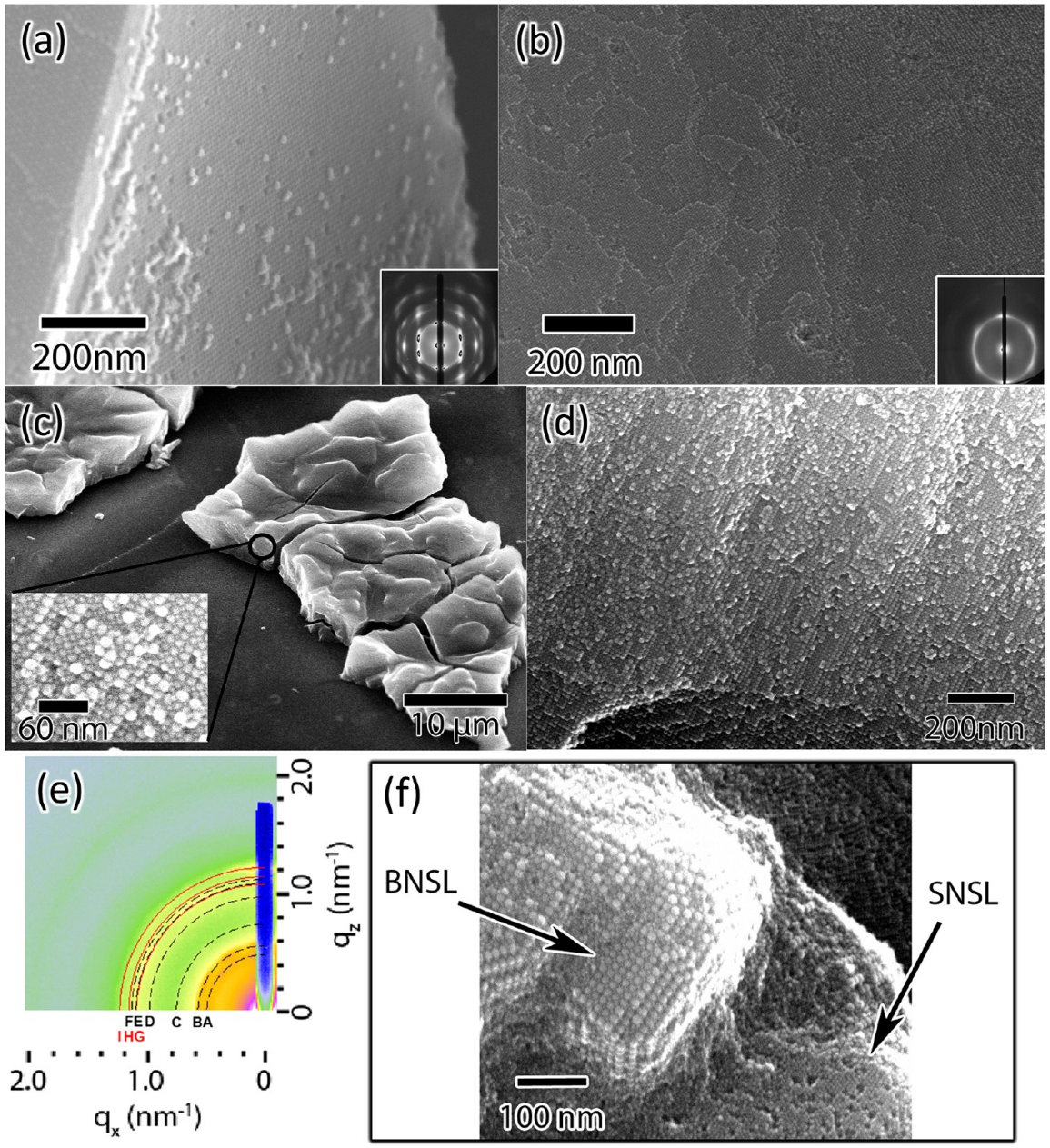

Figure 1. (a) SEM images of the side of one piece of the dried 13.8 nm iron oxide NP SNSL film, with the SAXS pattern inset suggesting *fcc* structure. (b) SEM images the top-view of the 5.9 nm iron oxide NP SNSL, with the SAXS pattern suggesting *hcp* structure. (c) SEM image of BNSL pieces composed of 5.9 and 12.4 nm iron oxide NPs. (d) Cross section SEM image of a large single crystalline domain of the BNSL in (c) over 1 μm. (e) SAXS diffraction pattern showing a mixture of BNSL and SNSL structures in (c). The indexed peaks are noted as dashed black arcs: A(001), B(100), C(101), D(002)/(110) (degenerate), E(102), and F(111) for the *sh* BNSL; solid red arcs: G(100), H(101), and I(002) for the *hcp* SNSL. Lattice constants for the *sh* are $a = b = 15.0$ nm, $c = 15.0$ nm; for the *hcp* they are $a = b = 7.8$ nm, $c = 12.7$ nm. This pattern is obtained with the beam normal to the substrate. No lattice distortion is observed, in contrast to that seen in samples described in Figures 2 and 4. (f) SEM image of (c) showing the BNSL and the 5.9 nm NP SNSL coexist in close proximity in one sample.

monolithic SNSL pieces from 13.8 nm diameter iron oxide NPs, with average ~50 μm lateral dimension and ~10 μm thickness. The Figure 1a inset shows the SAXS pattern for SNSLs of 13.8 nm NPs, which is indexed to a face-centered cubic (*fcc*) structure, as are the SNSLs of NPs examined with diameters ≥10.6 nm; also see Figure S2a,b. Particles examined with diameter ≤8.0 nm form the hexagonal close-packed (*hcp*) structure, such as the SNSLs of 5.9 nm diameter NPs shown in Figures 1b and S2c. This structure difference is attributed to the different strengths of anisotropic interactions of these NPs. In a hard sphere model, the *fcc* structure is thermodynamically more stable than the *hcp* structure, because the different packing order causes an entropy difference[31] estimated to be on the order of 10^{-3} k_B per NP. Anisotropic interactions, such as due to NP electric dipoles or magnetic dipoles, would lower the energy by aligning the A and C layers, to favor the *hcp* (ABABAB...) structure over the *fcc* (ABCABC...) structure. We believe the observed *hcp* structure in 5.9 nm NP SNSLs is due to stronger anisotropic interactions, electric and/or magnetic dipole interactions that override the entropy contribution. Anisotropic dipole interactions are known to be strong enough to enable NPs to stack in symmetries not expected in hard

dx.doi.org/10.1021/ja307848h | *J. Am. Chem. Soc.* 2012, 134, 18732−18738

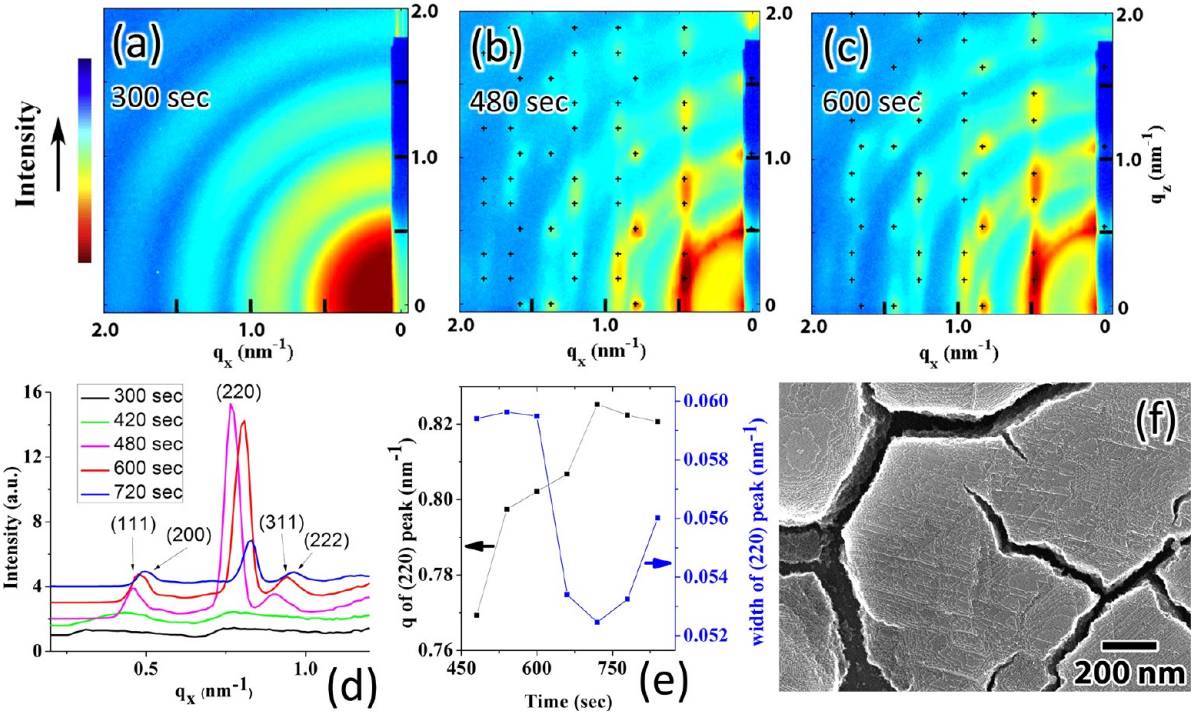

Figure 2. SAXS patterns during SNSL drying, with (a–c) SAXS patterns of 13.8 nm iron oxide NP solution during solvent drying, sampled at 300, 480, and 600 s, respectively. The peaks are indexed to *fcc* compressed along the [111] direction, with a = 22.5 nm and 6% compression in (b) and with a = 21.5 nm and 7% compression in (c). The SLs are highly oriented, with the (111) plane parallel to the substrate. Complete indexing can be found in the Figure S4. (d) Evolution of the structure factor peaks along the q_x axis. (The structure factor is the quotient of the diffraction pattern and the form factor, which is taken as the SAXS pattern at 240 s.) Note the glassy stage hump at q_x ~0.4 nm^{-1}, on the 420 s green curve before the SL forms. The structure factor at 300 s is flat, indicating that there is no ordering in the NP solution. (e) Evolution of the q_x peak value and width of the (220) peak. (f) SEM images showing the SL cracks after the solvent evaporates, which explains the increase of the peak width at the final stages of drying.

sphere models.[32] In future work we will examine if the packing symmetry can be changed by varying external fields.[33]

The conditions for growing BNSLs from 12.4 and 5.9 nm iron oxide NPs were also determined, as shown in Figure 1c,d,f (SEM images), and e (diffraction pattern). The ratio of the solution concentrations of the 5.9 and 12.4 nm NPs for the SAXS study was targeted at the 2:1 needed for AlB_2 stacking. An SEM survey of the sample after solvent drying revealed the formation of both the BNSL and a 5.9 nm NP SNSL (Figure 1f), with no 12.4 nm NP SNSL formation, so the initial solution ratio was in fact >2:1. This allows a direct comparison between the growth kinetics of SNSLs and BNSLs, which will be discussed later. The structure of the BNSL is indexed to be *simple hexagonal* (AlB_2 isostructure), as is confirmed by the SEM images in Figure S3. Upon adding extra 12.4 nm particles to this solution so the ratio would be <2:1, SEM analysis showed that only the BNSL and 12.4 nm NP SNSL form. This indicates that forming the AlB_2 BNSL is favored over the separate formation of SNSLs of these two NPs.

Obtaining large 3D BNSLs by drop casting has been difficult. We believe our success in forming them is due to more careful solvent evaporation control, with suitably slowed evaporation at the critical stage of NP ordering. The BNSLs are smaller than the SNSLs we formed from a single component, as seen by SEM and SAXS (with ring patterns for the BNSLs and dot patterns for the SNSLs). This may be due to disruptions by the NP expulsion described below.

Monitoring SNSL Growth by SAXS. With the desired growth conditions established, we used SAXS to probe the growth in real time. Figure 2a–c (and Movie S1) show a series of diffraction patterns collected during the growth of 13.8 nm NP SNSLs. The diffraction pattern evolves from the form factor of randomly positioned NPs in solution to strong diffraction spots, which are indexed to highly oriented *fcc* structures (Figure S4). This shows that the (111) plane is oriented parallel to the substrate, which is confirmed by a survey over large areas by SEM. We believe this orientation occurs because the growth of the 3D SL starts with 2D arrays at the top liquid surface, which then grow/stack in the vertical direction. Such 2D NP packing at the liquid surface has been reported many times for NP self-assembly.[3,8,27]

The diffraction spots showed a q-value increase during the evolution (Movie S1), which indicates a lattice contraction. After dividing the SAXS patterns by the form factor (the SAXS pattern at 240 s), we obtained the structure factor of the SL, which gives us more details of the evolution of SL. Figure 2d shows the evolution of the structure factor peaks along the q_x axis, and Figure 2e shows the evolution of the peak position and width of the (220) planes. The in-plane q increases by ~0.056 nm^{-1}, i.e., a ~0.55 nm contraction between the (220) planes. Such lattice contraction is consistent with earlier reports on 2D and 3D NP superlattice growth.[26,27] The peak width decreases from 0.0594 to 0.0525 nm^{-1} and then increases to 0.0560 nm^{-1}, which suggests that while the SNSL lattice constant is decreasing during drying, the SNSL grows in size and then cracks into smaller pieces. The final cracking of the SNSL was also confirmed by SEM images (Figure 2f). As has been seen earlier,[17,27] this cracking may be due to strain arising from the adhesion between the 3D SNSL and the substrate,

dx.doi.org/10.1021/ja307848h | J. Am. Chem. Soc. 2012, 134, 18732–18738

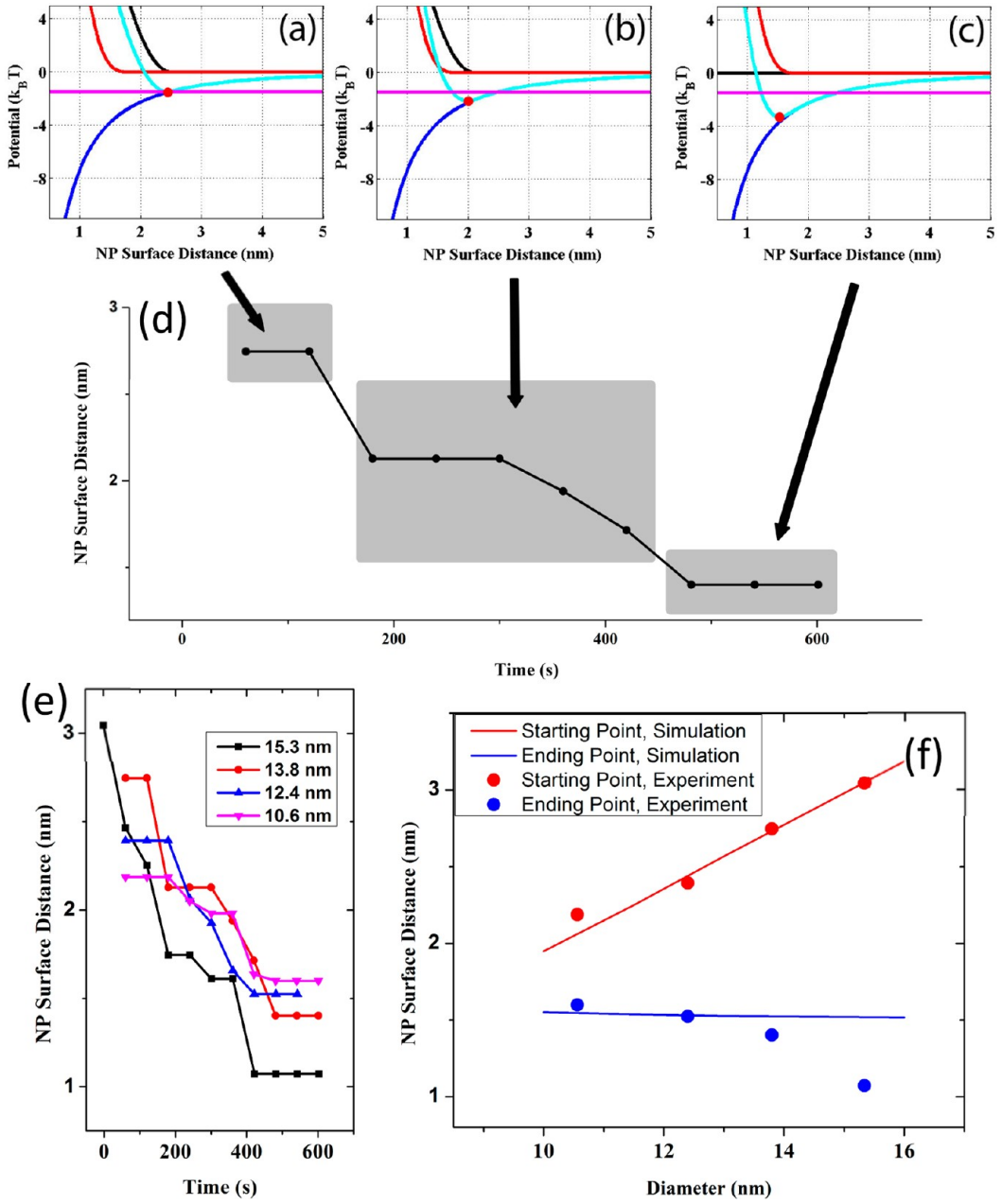

Figure 3. Analysis of NP separations during drying of SNSLs, with (a–c) modeling of the interaction energies as solvent continues to evaporate, when (a) the SL growth starts, (b) the SL contracts, and (c) SL contraction ends, for 12.4 nm iron oxide NP SNSLs. The energy minimum (red dot) equals the Brownian motion energy (3/2 $k_B T$) when NP ordering starts in (a). The SL contraction ends when all solvent has evaporated, represented by a zero osmotic potential (black line) in (c). The blue, black, red, cyan, and purple lines are the vdW energy, osmotic potential, ligand elastic energy, sum of these three, and the Brownian motion energy, respectively. (d,e) Evolution of the NP surface separation during solvent evaporation for (d) 12.4 nm NPs and (e) 15.3 (black), 13.8 (red), 12.4 (blue), and 10.6 nm (purple) NPs. (f) Fitting of the starting (blue) and ending (red) NP surface distances of SL growth. A Hamaker constant of ~21 zJ for iron oxide was obtained by fitting NP separations when precipitation starts.

which may also be the cause of the observed ~6–8% vertical compression.

We studied the growth of *fcc* SNSLs of NPs from 10.6 to 15.3 nm diameter by indexing the structure factor images of the diffraction patterns to obtain the lattice constants and distances between the surfaces of nearest-neighbor NPs during solvent evaporation. SNSLs of NPs smaller than 10 nm were not included for comparison here because of their different symmetry, *hcp*. Details of the indexing method can be found in Figure S4. The nearest-neighbor NP core separations are plotted versus time, corresponding to drying stages (Figure 3d). These values exhibit an unanticipated crossing behavior, in which larger NPs start ordering when they are farther apart and complete crystallization closer together than those of smaller NPs.

Modeling SNSL Formation. We explain the SNSL formation by comparing the interaction potentials between NPs, including those due to van der Waals (vdW) interactions (Φ_{vdW}), osmotic pressure from the mixing of solvent and ligands (Φ_{osm}), and elastic repulsion between the ligands on nearest neighbor NP cores (Φ_{elas}), with the Brownian motion energy, 3/2 $k_B T$ per NP; NP crystallization occurs when the net

dx.doi.org/10.1021/ja307848h | J. Am. Chem. Soc. 2012, 134, 18732–18738

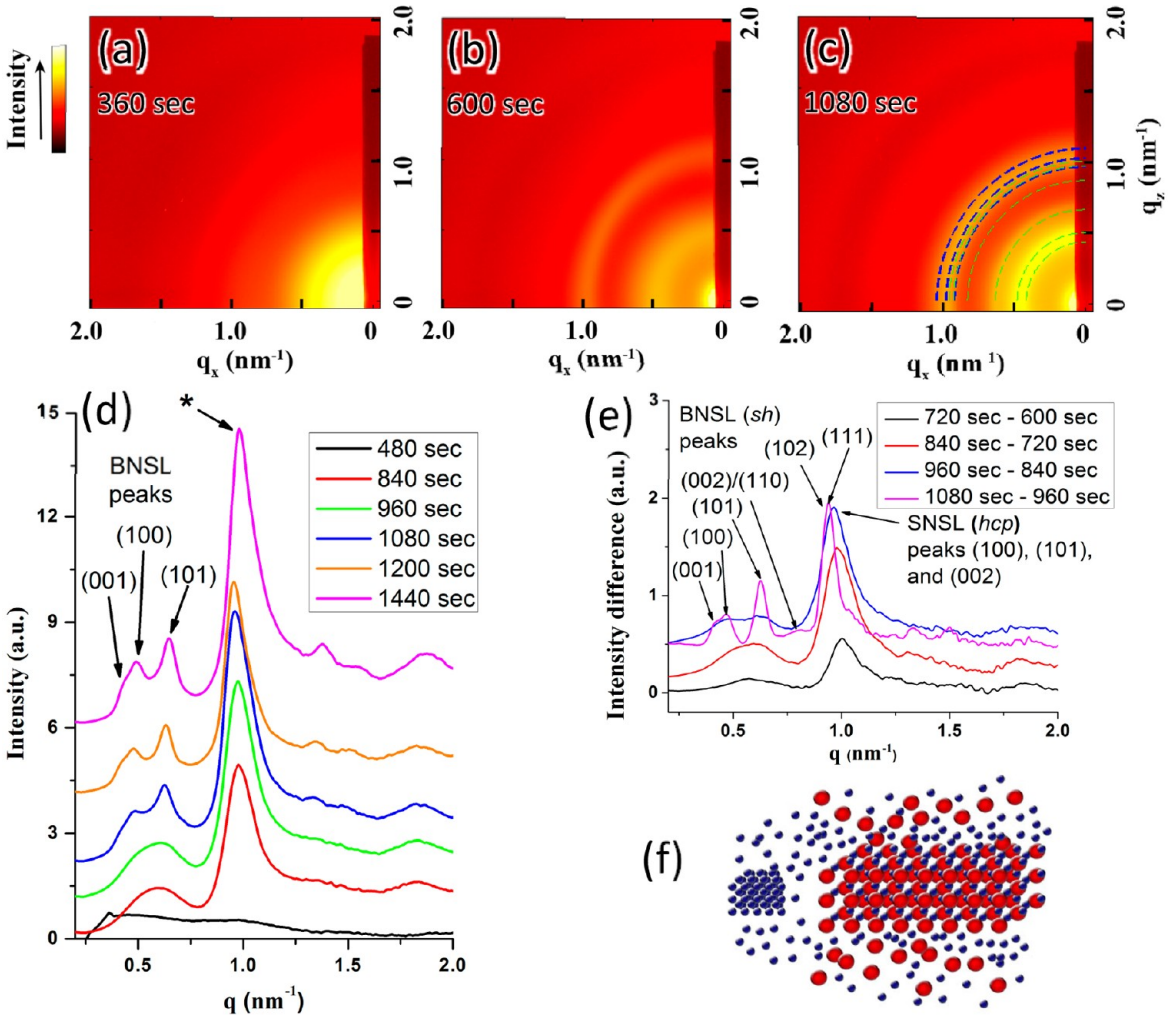

Figure 4. (a–c) SAXS evolution of the binary NP mixture film during solvent evaporation to form BNSLs, with 5.9 and 12.4 nm iron oxide NPs mixed with ~2:1 ratio in the drop cast solution. Ordering occurs first with the 5.9 nm NP SNSL at 600 s in (b) and then with the BNSL at 1080 s in (c). The 5.9 nm NP SNSL forms the *hcp* structure, and the BNSL forms a *sh* structure (AlB_2 type). The indexed peaks are the following: dashed green arcs (001), (100), (101), (002)/(110) (degenerate), (102), and (111) for the *sh* BNSL; dashed blue arcs (100), (101), and (002) for the *hcp* SNSL. The lattice constants are obtained by fitting the radially integrated peaks in (d), which for the *sh* are $a = b = 15.3$ nm, $c = 15.3$ nm, and for the *hcp* are $a = b = 7.9$ nm, $c = 12.9$ nm. This pattern is obtained with the beam hitting the substrate at a 0.4° angle. 5% lattice compression is observed along the *z*-axis, which is included in the radial integration and indexing. (d) Evolution of the radially integrated structure factor peaks of the binary NP SL assembly. The structure factor is the quotient of the diffraction pattern and the form factor (which is the pattern at 360 s). The first three peaks of the BNSL can be identified, and the SNSL peaks overlap higher-order BNSL peaks to form the peak denoted by *. (e) Differences of successive traces in (d), which indicate peak growth at different stages. Growth of the BNSL peaks at 1080 s is evident. (f) Schematic of the process of the expulsion of smaller 5.9 nm NPs from the binary NP mixture as it forms a 2:1 ratio of the 5.9:12.4 nm NPs in the AlB_2-type BNSL stacking.

attraction energy exceeds the kinetic energy per NP. The potential profiles for pairs of NPs were determined using eqs S2–S4.[34]

Figure 3a compares the energies of the different interactions between 12.4 nm NPs (6× each energy in eqs S2–S4, to account for the 12 nearest neighbors of each NP, without double counting) and their sum when there is sufficient solvent evaporation for the onset of precipitation, which is when this interaction energy first equals the Brownian motion energy, 3/2 k_BT per NP. Additional removal of solvent thins the effective ligand shell further, which causes the minimum of the total potential curve to dip below the Brownian motion energy at even smaller NP separations, enabling continued precipitation of NPs from solution (Figure 3b). Larger NPs precipitate when they are farther apart than smaller NPs because of their stronger core–core vdW forces and when they precipitate slowly enough, as here, in the energetically more favorable SNSL structure. The solvent system, consisting of three solvents with very different vapor pressures, slows down the drying, which allows the precipitated NPs to reach equilibrium, i.e., to attain ordered close packing rather than glass-like packing. An SEM survey over very large areas confirms the SNSL structure to be dominant over randomly packed NPs, although initially there is a glass-like stage (Figure 2d). The final distance between NP core surfaces is determined by the NP vdW attraction and ligand repulsions in the absence of solvent (Figure 3c), where the stronger vdW forces of the larger NPs compress the ligands more, leading to smaller surface–surface NP distances than those of smaller NPs with the same ligand structure. This evolution is also described in Movie S2. These observations and model predictions are also consistent with the well-known difficulty of dissolving larger NPs.

dx.doi.org/10.1021/ja307848h | *J. Am. Chem. Soc.* 2012, 134, 18732–18738

The NP surface distance is plotted in Figure 3d,e during evaporation for the four particle sizes examined. The starting and ending separations are plotted in Figure 3f, along with model predictions (analogs of Figure 3a,c for each NP size) fit with a Hamaker constant of ∼21 zJ, which is in good agreement with recent theoretical prediction (9−29 zJ for iron oxides).[35] We found that the starting point of NP precipitation is sensitive to the value of the Hamaker constant and the effective ligand shell thickness in the osmotic pressure curve, which depends on the extent of solvent evaporation, because of the shape of this curve and effectively the balance between the vdW and Brownian motion energies. The agreement between the experimental and model of final NP separation is poorer for larger NPs. This could be due to increased ligand protrusion into NP interstitial regions for larger NPs caused by the relatively stronger vdW interactions that lead to closer NPs. Also, the model predicts the distances between NPs for unstrained films, so small deviations from the model can be expected during the intermediate stages of drying before cracking.

Monitoring BNSL Growth by SAXS. The kinetics of the growth of the BNSLs were also studied. Figure 4a−c (and Movie S3) shows the evolution of SAXS diffraction patterns for drop casting the 5.9/12.4 nm iron oxide NP mixture that was also used for Figure 1c−f. As seen by SEM, the BNSL and a 5.9 nm NP SNSL form, as indicated by the evolution of the radially integrated structure factor peaks in Figure 4d. The differences of successive scans plotted in Figure 4e reveal more clearly the differences in BNSL and 5.9 nm NP SNSL formation. The first three difference curves spanning from 600 to 960 s show a growing but broad feature of merged BNSL peaks, suggesting only continued local ordering. Concurrently, the intensity of the relatively sharp peak at ∼1.0 nm^{-1} increases rapidly, suggesting growth of the 5.9 nm NP SNSL with long-range ordering. From 960 to 1080 s, sharp BNSL peaks appear, suggesting relatively rapid long-range ordering, and there is no longer an increase in the SNSL peak. This suggests that the SNSL growth has stopped by the time long-range ordering in the BNSL has started. This likely means that long-range BNSL growth begins only when the local NP ratio is precisely 2:1 or, in this case, after the smaller NPs have been expelled and grew relatively rapidly into SNSLs. Figure 4f is a schematic of SL formation and NP repulsion. The expulsion of the stoichiometric excess of smaller NPs (from ∼600 to 960 s in Figure 4e) takes longer than the growth of the long-range ordering of the SNSLs (within each 120 s segment from 600 to 960 s, as limited by the rate of expulsion of the smaller NPs) and BNSLs (within the 120 s segment from 960 to 1080 s).

CONCLUSIONS

We used real-time SAXS to explain the kinetics of growth of thick NP superlattices. Controlling the conditions of solvent evaporation, by using a three-solvent system and controlling the solvent pressure, enables the growth of very thick superlattices, within a time frame suitable for SAXS analysis. For the iron oxide (magnetite) NP SLs studied here, the larger the NP, the farther apart are the NPs when the SNSLs begin to precipitate and the closer they are after ordering. This is understood by using a model that compares NP interaction energies and kinetic energy during solvent evaporation. A Hamaker constant of ∼21 zJ was experimentally determined by fitting the NP distances in this model. This technique could be extended to other specific NP systems to evaluate interactions at the nanoscale, which would be difficult to do otherwise. When forming BNSLs of two different sized NPs, the NPs that are in excess of that needed to achieve the final BNSL stoichiometry are expelled during the BNSL formation, and these expelled NPs can form SNSLs. The long-range ordering of these SNSLs and the BNSLs can occur faster than the NP expulsion. This understanding can be very helpful in controlling NP self-assembly, permitting rational design of multicomponent NP SLs.

ASSOCIATED CONTENT

Supporting Information

NP synthesis and assembly details; SEMS of the SLs; methods for determining NP size and SNSL indexing using SAXS; SAXS movies of SNSL and BNSL formation; details of the potentials used in the SL assembly model; and a movie of the potentials during assembly. This material is available free of charge via the Internet at http://pubs.acs.org.

AUTHOR INFORMATION

Corresponding Author

CL2551@columbia.edu; IPH1@columbia.edu

Notes

The authors declare no competing financial interest.

ACKNOWLEDGMENTS

We thank Youjin Lee and Theodore Kramer for helpful discussion. Support was provided by the MRSEC program of the National Science Foundation (DMR-0213574) (I.P.H.), the NSEC program of the NSF (CHE-0641523) (A.J.A.), the EFRC program of DoE (DE-SC0001085) (C.L. and D.Z), by the New York State Office of Science, Technology, and Academic Research, and a gift by the Honda Research Institute. Use of the National Synchrotron Light Source, Brookhaven National Laboratory, was supported by the U.S. Department of Energy, Office of Science, Office of Basic Energy Sciences, under contract no. DE-AC02-98CH10886.

REFERENCES

(1) Talapin, D. V.; Lee, J. S.; Kovalenko, M. V.; Shevchenko, E. V. *Chem. Rev.* **2010**, *110*, 389−458.
(2) Kovalenko, M. V.; Bodnarchuk, M. I.; Talapin, D. V. *J. Am. Chem. Soc.* **2010**, *132*, 15124−15126.
(3) Dong, A. G.; Chen, J.; Vora, P. M.; Kikkawa, J. M.; Murray, C. B. *Nature* **2010**, *466*, 474−477.
(4) Park, S. Y.; Lytton-Jean, A. K. R.; Lee, B.; Weigand, S.; Schatz, G. C.; Mirkin, C. A. *Nature* **2008**, *451*, 553−556.
(5) Nykypanchuk, D.; Maye, M. M.; van der Lelie, D.; Gang, O. *Nature* **2008**, *451*, 549−552.
(6) Kalsin, A. M.; Fialkowski, M.; Paszewski, M.; Smoukov, S. K.; Bishop, K. J. M.; Grzybowski, B. A. *Science* **2006**, *312*, 420−424.
(7) Bodnarchuk, M. I.; Li, L.; Fok, A.; Nachtergaele, S.; Ismagilov, R. F.; Talapin, D. V. *J. Am. Chem. Soc.* **2011**, *133*, 8956−8960.
(8) Bigioni, T. P.; Lin, X. M.; Nguyen, T. T.; Corwin, E. I.; Witten, T. A.; Jaeger, H. M. *Nat. Mater.* **2006**, *5*, 265−270.
(9) Talapin, D. V.; Shevchenko, E. V.; Murray, C. B.; Kornowski, A.; Forster, S.; Weller, H. *J. Am. Chem. Soc.* **2004**, *126*, 12984−12988.
(10) Henzie, J.; Grünwald, M.; Widmer-Cooper, A.; Geissler, P. L.; Yang, P. *Nat. Mater.* **2012**, *11*, 131−137.
(11) Quan, Z. W.; Fang, J. Y. *Nano Today* **2010**, *5*, 390−411.
(12) Dong, A.; Ye, X.; Chen, J.; Murray, C. B. *Nano Lett.* **2011**, *11*, 1804−1809.
(13) Evers, W. H.; Friedrich, H.; Filion, L.; Dijkstra, M.; Vanmaekelbergh, D. *Angew. Chem., Int. Ed.* **2009**, *48*, 9655−9657.

(14) Tang, Z. Y.; Zhang, Z. L.; Wang, Y.; Glotzer, S. C.; Kotov, N. A. *Science* **2006**, *314*, 274−278.
(15) Talapin, D. V.; Shevchenko, E. V.; Bodnarchuk, M. I.; Ye, X. C.; Chen, J.; Murray, C. B. *Nature* **2009**, *461*, 964−967.
(16) Bodnarchuk, M. I.; Kovalenko, M. V.; Heiss, W.; Talapin, D. V. *J. Am. Chem. Soc.* **2010**, *132*, 11967−11977.
(17) Smith, D. K.; Goodfellow, B.; Smilgies, D. M.; Korgel, B. A. *J. Am. Chem. Soc.* **2009**, *131*, 3281−3290.
(18) Choi, J. J.; Bealing, C. R.; Bian, K. F.; Hughes, K. J.; Zhang, W. Y.; Smilgies, D. M.; Hennig, R. G.; Engstrom, J. R.; Hanrath, T. *J. Am. Chem. Soc.* **2011**, *133*, 3131−3138.
(19) Bodnarchuk, M. I.; Sheychenko, E. V.; Talapin, D. V. *J. Am. Chem. Soc.* **2011**, *133*, 20837−20849.
(20) Chen, Z. Y.; Moore, J.; Radtke, G.; Sirringhaus, H.; O'Brien, S. *J. Am. Chem. Soc.* **2007**, *129*, 15702−15709.
(21) Lee, B.; Podsiadlo, P.; Rupich, S.; Talapin, D. V.; Rajh, T.; Shevchenko, E. V. *J. Am. Chem. Soc.* **2009**, *131*, 16386−16388.
(22) Ge, G.; Brus, L. E. *Nano Lett.* **2001**, *1*, 219−222.
(23) Yang, L.; Gao, K. Y.; Luo, Y. H.; Luo, J. H.; Li, D. M.; Meng, Q. B. *Langmuir* **2011**, *27*, 1700−1706.
(24) Park, J.; Zheng, H.; Lee, W. C.; Geissler, P. L.; Rabani, E.; Alivisatos, A. P. *ACS Nano* **2012**, *6*, 2078−2085.
(25) Abecassis, B.; Testard, F.; Spalla, O. *Phys. Rev. Lett.* **2008**, *100*, 115504.
(26) Connolly, S.; Fullam, S.; Korgel, B.; Fitzmaurice, D. *J. Am. Chem. Soc.* **1998**, *120*, 2969−2970.
(27) Jiang, Z.; Lin, X. M.; Sprung, M.; Narayanan, S.; Wang, J. *Nano Lett.* **2010**, *10*, 799−803.
(28) Hyeon, T.; Lee, S. S.; Park, J.; Chung, Y.; Bin Na, H. *J. Am. Chem. Soc.* **2001**, *123*, 12798−12801.
(29) Lu, C.; Chen, Z.; O'Brien, S. *Chem. Mater.* **2008**, *20*, 3594−3600.
(30) Akey, A.; Lu, C. G.; Yang, L.; Herman, I. P. *Nano Lett.* **2010**, *10*, 1517−1521.
(31) Bolhuis, P. G.; Frenkel, D.; Mau, S. C.; Huse, D. A. *Nature* **1997**, *388*, 235−236.
(32) Talapin, D. V.; Shevchenko, E. V.; Murray, C. B.; Titov, A. V.; Kral, P. *Nano Lett.* **2007**, *7*, 1213−1219.
(33) Ryan, K. M.; Mastroianni, A.; Stancil, K. A.; Liu, H.; Alivisatos, A. P. *Nano Lett.* **2006**, *6*, 1479−1482.
(34) Saunders, S. R.; Eden, M. R.; Roberts, C. B. *J. Phys. Chem. C* **2011**, *115*, 4603−4610.
(35) Faure, B.; Salazar-Alvarez, G.; Bergström, L. *Langmuir* **2011**, *27*, 8659−8664.
(36) Lu, C.; Akey, A. A.; Herman, I. P. *Appl. Phys. Lett.* **2012**, *101*, 133109.